Edge Preserving and Noise Reducing Reconstruction for Magnetic Particle Imaging

Martin Storath*, Christina Brandt, Martin Hofmann, Tobias Knopp, Johannes Salamon, Alexander Weber, and Andreas Weinmann

***Abstract*— Magnetic particle imaging (MPI) is an emerging medical imaging modality which is based on the non-linear response of magnetic nanoparticles to an applied magnetic field. It is an important feature of MPI that even fast dynamic processes can be captured for 3D volumes. The high temporal resolution in turn leads to large amounts of data which have to be handled efficiently. But as the system matrix of MPI is non-sparse, the image reconstruction gets computationally demanding. Therefore, currently only basic image reconstruction methods such as Tikhonov regularization are used. However, Tikhonov regularization is known to oversmooth edges in the reconstructed image and to have only a limited noise reducing effect. In this work, we develop an efficient edge preserving and noise reducing reconstruction method for MPI. As regularization model, we propose to use the nonnegative fused lasso model, and we devise a discretization that is adapted to the acquisition geometry of the preclinical MPI scanner considered in this work. We develop a customized solver based on a generalized forward-backward scheme which is particularly suitable for the dense and not well-structured system matrices in MPI. Already a non-optimized prototype implementation processes a 3D volume within a few seconds so that processing several frames per second seems amenable. We demonstrate the improvement in reconstruction quality over the state-of-the-art method in an experimental medical setup for an in-vitro angioplasty of a stenosis.**

***Index Terms*— Angioplasty, edge preserving regularization, forward backward splitting, fused lasso, magnetic particle imaging.**

Manuscript received May 18, 2016; revised July 19, 2016; accepted July 20, 2016. Date of publication July 22, 2016; date of current version December 29, 2016. This work was supported by the German Research Foundation (project ER777/1-1). C. Brandt was supported by the Academy of Finland (project 286964). M. Hofmann and T. Knopp acknowledge funding and support of the German Research Foundation (DFG, grant no. AD125/5-1). A. Weber acknowledges the financial support by the German Federal Ministry of Education and Research (FKZ 13N11088). A. Weinmann was supported by the Helmholtz Association (VH-NG-526). *Asterisk indicates corresponding author.*

*M. Storath is with Image Analysis and Learning Group, Universität Heidelberg, 69120 Heidelberg, Germany.

C. Brandt is with the Inverse Problems Group, University of Eastern Finland, 49076 Kuopio, Finland.

M. Hofmann and T. Knopp are with the Section for Biomedical Imaging, University Medical Center Hamburg-Eppendorf, and with the Institute for Biomedical Imaging, Hamburg University of Technology, 20246 Hamburg, Germany.

J. Salamon is with the Department of Diagnostic and Interventional Radiology, University Medical Center Hamburg-Eppendorf, 20246 Hamburg, Germany.

A. Weber is with Bruker Biospin, 76275 Ettlingen, and also with the Institute of Medical Engineering, University of Lübeck, 23562 Lübeck, Germany.

A. Weinmann is with the Fast Algorithms for Biomedical Imaging Group, Helmholtz Zentrum München, with the Technische Universität München, and with the Darmstadt University of Applied Sciences, 64295 Darmstadt, Germany.

Digital Object Identifier 10.1109/TMI.2016.2593954

I. Introduction

MAGNETIC particle imaging (MPI) is an emerging imaging modality that determines the concentration of magnetic nanoparticles by measuring their non-linear magnetization response to an applied magnetic field [1], [2]. MPI offers a high spatial and temporal resolution and, in contrast to other tomographic methods, it does not employ any ionizing radiation. One of the main benefits is that it is able to capture fast dynamic processes in-vivo and in 3D [3]. This makes MPI a very promising imaging modality for biomedical applications, for example visualization of instruments for cardiovascular intervention [4], [5].

In MPI, the desired particle concentration is measured indirectly via an induced current in the receive coils; the relation between the density and the current is described by the system function. The reconstruction of the concentration from the acquired data is an ill-posed inverse problem [6]: even small noise in the data can lead to large errors in the reconstruction. Therefore, the reconstruction requires regularization. Currently, the state-of-the-art method is based on Tikhonov regularization [3], [7]. As Tikhonov regularization can be carried out by solving a linear system of equations, it is fast, particularly simple to implement, and many solvers are available such as the conjugate gradients method and the Kaczmarz method. On the downside, the Tikhonov model has only limited noise suppression capabilities, it severely diminishes the contrast, and it smoothes out the edges. This directly hampers possible medical applications like vessel visualization, bolus tracking, and the guidance of medical devices. These drawbacks can be overcome by using priors based on the ℓ^1-norm. In particular, total variation (TV) [8], [9] and lasso regularization [10], [11] have been used for various imaging modalities [12]–[14]. These models match with the typical statistical properties of images significantly better than Tikhonov regularization. On the flipside, these regularization methods are computationally more demanding making their implementation for MPI a challenging task.

We note that the present paper deals with rapid 1D-3D MPI sequences, where the sampling trajectory is a Lissajous curve

leading to a complex structure of the system matrix which is challenging to model and therefore usually measured [15]. For Cartesian sequences as used in [16]–[18], the MPI signal chain can be formulated by a simple coordinate transformation in combination with a spatial convolution. The state-of-of-the art reconstruction methods [19] for these types of sequences usually do not formulate the reconstruction problem in an inverse setting.

A. Contributions

In this work, we propose an new image reconstruction method particularly suitable for magnetic particle imaging. We address the following three objectives: *(i)* to find a regularization model that gives better reconstructions of the particle densities than the state-of-the-art method; *(ii)* to derive a solver for that model which is efficient for the dense and not well-structured system matrices appearing in MPI; *(iii)* to demonstrate the advantages for an experimental in-vitro angioplasty imaged by MPI.

Towards the first goal *(i)*, we propose to utilize mixed ℓ^1/lasso and total variation (TV) regularizing terms for the reconstruction process, which is known as *fused lasso model* in statistics [20]. The priors promote sparsity for both the reconstructed image and its gradient, and they better match with the typical statistical properties of MPI images. To account for the physical properties of a particle density, we utilize additionally a non-negativity constraint. In a series of synthetic experiments with known ground truth, we demonstrate that the non-negative fused lasso model yields higher reconstruction quality than the state-of-the-art method with respect to signal-to-noise ratio and visual inspection.

Towards the second goal *(ii)*, we first propose to adopt a near-isotropic discretization, originally developed by the authors for Potts priors [21], [22], which takes into account the usually non-isotropic spatial resolution of MPI. This is due to the gradient strength of the applied magnetic gradient field being twice as high in a particular direction (up-down for the preclinical system considered in this work). Based on that discretization, we propose a novel splitting of the functional into a data term, a non-negativity term, and a set of pathwise fused lasso terms. We utilize the generalized forward backward scheme of Raguet et al. [23] to minimize the resulting split functional. In contrast to other popular optimization schemes [24], [25], it employs a gradient descent step with respect to the data term instead of a proximal mapping. Since the gradient step is much cheaper to compute than the proximal mapping (matrix-vector multiplication vs. solving a linear system of equations) it is particularly suitable for the dense system matrices appearing in MPI. On the other hand, our specific splitting requires evaluation of proximal mappings with respect to pathwise fused lasso terms. But these can be solved efficiently in linear complexity [26], [27]. Furthermore, the method is highly parallelizable. For time-lapse data, we utilize a warmstarting strategy; to this end, we use the previous result as initial guess for the next frame. Due to the high temporal resolution of MPI, and thus little changes between two consecutive frames, we obtain high quality within only a few iterations.

For the last goal *(iii)*, we evaluate our method in an experimental medical setup for MPI, an in-vitro angioplasty of a stenosis. To this end, we took measurements of an inflating balloon catheter in a vessel phantom with induced stenosis using a preclinical MPI scanner. The resulting images have better reconstruction quality (both with respect to signal-to-noise ratio and visual inspection) than the state-of-the-art method. The computation time is only moderately higher than that of the state-of-the-art method.

B. Organization of the Paper

The paper is organized as follows. We first describe the mathematical model for the measurement process and the state-of-the-art regularization in Section II. In Section III, we motivate the proposed regularization model for MPI. In Section IV we derive our new splitting algorithm. To this end, we introduce a near-isotropic discretization of the TV semi-norm in Section IV-A and propose a generalized forward backward splitting approach for the computation of the minimizer of our regularization model in Subsection IV-B. We then explain how to efficiently solve the subproblems in Subsection IV-C and present our complete algorithm in Subsection IV-D. In Section V, we drive a simulation study on synthetic data. In Section VI, we demonstrate the practical performance of our approach for in-vitro angioplasty of a stenosis.

II. Measurement Process of Magnetic Particle Imaging and State-of-the-Art Image Reconstruction

A. Measurement Process in MPI

The goal of MPI is to reconstruct the density ν of iron oxide particles contained in an object of interest, e.g., in a blood vessel or in a catheter. We briefly describe the basic principle of a field-free point (FFP) scanner; for a comprehensive treatment we refer to the book [28]. A specific magnetic field is set up which saturates the nanoparticles in all the field of view except in the neighborhood of a single point, called the FFP. During the imaging process, the FFP is moved over the object. This changes the magnetization of the nanoparticles and induces a current in a set of receive coils. The relation between the particle concentration ν and the measurements f can be described by a linear mapping A called the system function. The system function has been analyzed in [29], [30]. Although first models exists for the system function currently the best results are obtained by the measurement based approach [15], [19], [31]. That is, the system function is obtained by measuring the system response of a delta probe at every voxel.

We will consider MPI reconstruction in the $1D$, the $2D$, and the $3D$ space domains, i.e. a reconstructed signal/image $u^\#$ lives in the space $X = \mathbb{R}^{n_1}$, $X = \mathbb{R}^{n_1 \times n_2}$ or $X = \mathbb{R}^{n_1 \times n_2 \times n_3}$. We denote the number of measurements by M and the total number of pixels/voxels by N; that is, $N = n_1$, $N = n_1 n_2$, or $N = n_1 n_2 n_3$, respectively. In the $1D$ case, we can directly identify the system function with a matrix $A \in \mathbb{R}^{M \times n_1}$ and so the measured data $f \in \mathbb{R}^M$ is given by $f = A\nu + \eta$, where ν denotes the true density and η is the noise on the

measurements. In order to avoid cumbersome notations, we will use the following convention for the $2D$ case. We denote by $\tilde{u} \in \mathbb{R}^{n_1 n_2}$ the (columnwise) vectorization of the image $u \in \mathbb{R}^{n_1 \times n_2}$. We associate A with matrix $\tilde{A} \in \mathbb{R}^{M \times N}$ such that $\tilde{A}\tilde{u} = Au$ for all $u \in \mathbb{R}^{n_1 \times n_2}$. Further, we denote the adjoint operator of A by A^*. In matrix notation, A^* is defined by $A^* g = \text{reshape}(\tilde{A}^T g)$ for $g \in \mathbb{R}^M$, where reshape is the inverse of the vectorization operation. We use an analogous notation for $3D$ images.

B. State-of-the-Art Reconstruction

As mentioned before, the reconstruction in MPI is an ill-posed inverse problem which is reflected in the rapid decay of the singular values of the system matrix [6]. Therefore, the image reconstruction requires regularization. Current reconstruction methods are based on Tikhonov-type regularization [3], [7], [29], [32]–[34]; that is, the reconstructed image u^ρ is the minimizer of an energy functional

$$u^\rho = \arg\min_u \rho \|u\|_2^2 + \|Au - f\|_2^2, \tag{1}$$

where $\|u\|_2^2 = \sum_{ijk} |u_{ijk}|^2$ (in the 3D setup). The optimization problem can be solved directly using QR decomposition or singular value decomposition. However, these methods are computationally too expensive for large system matrices, therefore in practice the corresponding normal equation is solved by an iterative method. To this end, most published papers that consider Lissajous type MPI sequences use the regularized Kaczmarz method (also called algebraic reconstruction technique) [3], [7], [29], [32]–[34]. The popularity of the Kaczmarz method can be explained by the following reasons. First, since the rows of the matrix A are known to be close to orthogonal, the Kaczmarz method converges rapidly, in most cases in less than ten iterations. Second, it easily allows to include non-negative constraints which typically improves the reconstruction result [3].

A refinement of the Tikhonov model (1) that is used in some publications [7], [33] is to introduce a diagonal weighting matrix W that weights the individual rows of the system matrix A and the measurement vector f. To this end the model (1) is adapted to include the system matrix $\tilde{A}' = W^{\frac{1}{2}}\tilde{A}$ and the data $\tilde{f}' = W^{\frac{1}{2}}\tilde{f}$ where W is the diagonal matrix consisting of the squared reciprocal of the row energy of $\tilde{A}$, i.e., $W = \text{diag}(1/w_1, \ldots, 1/w_M)$ with $w_i = \|\tilde{A}_{i,:}\|_2^2$. The weighting has two effects. First it can improve the reconstruction quality [7]. Second it can considerably improve the convergence rate of iterative solvers that apply multiplications with A during the reconstruction process. The idea is that frequency weighting has a similar effect as preconditioning and considerably improves the conditioning of the linear system [7]. Note that the Kaczmarz method does not necessarily require a weighting since the rows are inherently normalized within the algorithm.

III. Non-Negative Fused Lasso for Regularization in MPI

As mentioned in the introduction, the main advantage of Tikhonov regularization is its simplicity as it boils down a linear system of equations (possibly with non-negativity constraints). However, this simplicity comes at the cost of reconstruction quality. Loosely speaking, the penalty $\rho\|u\|_2^2$ in (1) which penalizes the total energy of the signal, primarily prevents the result from "blowing up" but it does not take into account any prior knowledge on the structure of the underlying image. In particular, spatial neighborhood structures are not reflected in the prior. The shortcomings of the regularization model become even more clear from a statistical perspective: Tikhonov regularization – known as ridge regression in statistics – is the maximum a posteriori (MAP) estimator for a Gaussian noise model and Gaussian prior. While the Gaussian model is a reasonable assumption for the measurement noise, the Gaussian prior is not well matched to the typical statistics of real images. The latter means that the reconstructed particle concentration is assumed to be independent and normally distributed with expectation zero. This, in particular, implies that neighboring pixel/voxel intensities are assumed to be uncorrelated. It has been observed that priors which take neighborhood structure into account are much better suited. A prominent example is the total variation (TV) prior [8]. In addition, this prior promotes the sparsity of the edge set. For these reasons we propose to use the TV prior. Another observation specific to MPI is that the particles concentrate often in a few spots within the field of view. In consequence, the number of non-zero voxels is often much smaller than the total number of voxels. This motivates to additionally employ a sparsity promoting prior. Furthermore, as the reconstructed image physically reflects a particle density, we impose non-negativity constraints. Note that non-negativity is a common assumption in MPI which typically leads to improved reconstruction quality, see e.g. [3], [15], [33]. Gathering these quantities, we propose the following variational model for regularization in MPI:

$$u^\# = \arg\min_{u \geq 0} \ \alpha \text{TV}(u) + \beta\|u\|_1 + \frac{1}{2}\|Au - f\|_2^2. \tag{2}$$

Here, $\text{TV}(u)$ denotes the total variation of u (which promotes sparse edge sets) and $\|u\|_1$ denotes the ℓ^1 norm of u (which penalizes non-zero intensities). The parameters $\alpha, \beta > 0$ control the relative weight of the regularizing terms. Model (2) without the non-negativity is known as *fused lasso* in the statistical literature [20]. Henceforth, we will refer to the model (2) as *non-negative fused lasso*.

Let us briefly discuss the gain of the model in the particularly simple 1D situation. In 1D, the discretization of the non-negative fused lasso has the explicit expression

$$u^\# = \arg\min_{u \in (\mathbb{R}_0^+)^n} \ \alpha \sum_i |u_{i+1} - u_i| + \beta \sum_i |u_i| + \frac{1}{2}\sum_i |(Au)_i - f_i|^2. \tag{3}$$

We compare the non-negative fused lasso reconstruction $u^\# \in \mathbb{R}^N$ for data $f \in \mathbb{R}^M$ to the state-of-the-art reconstruction for synthetic and for real 1D data in Fig. 1. (We note that we already use the 1D variant of the proposed algorithm here. We do this to give the reader an initial impression on the effects in the simple 1D setup. Details on the minimization scheme and the measurement setup will be given later on in Section V.) While Tikhonov regularization smoothes out

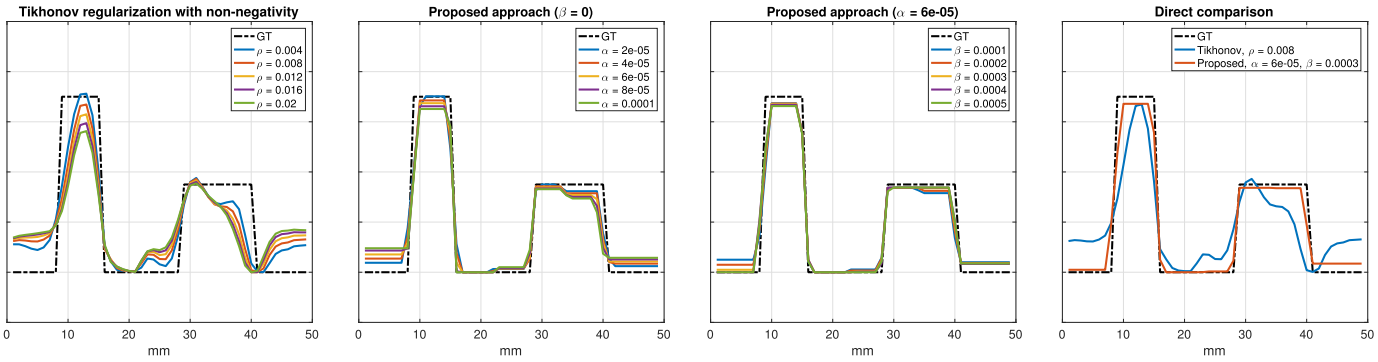

(a) Reconstruction from synthetic data.

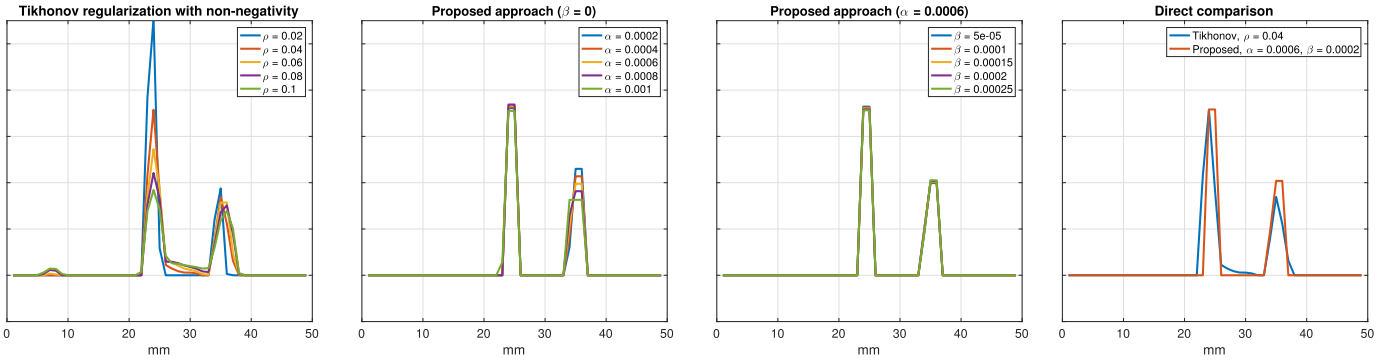

(b) Reconstruction from measured data of a physical phantom.

Fig. 1. Comparison of the proposed method to the state-of-the-art regularization. The top row shows simulated data with known ground truth. The bottom row displays reconstructions from measured data of a physical phantom. The phantom consists of two rods of diameter 4 mm in a 5 mm distance to each other, and the right rod has half of the concentration of the left one. The ordinate indicates the particle concentration in linear and arbitrary scale. In both cases Tikhonov regularization captures the two desired peaks but does not restore their homogeneous concentration (first column). Furthermore, for higher regularization parameters an extra spot appears. The total variation penalty produces sharply localized peaks with homogeneous interior (second column). The lasso/ℓ^1 term can improve the results further in particular at regions with zero concentration (third column, top). The last column shows direct comparisons.

the sharp transition between the zero particle density and the homogeneously positive density, the proposed non-negative fused lasso regularization recovers the sharp edges and homogeneous particle densities.

IV. Proposed Algorithm for Non-Negative Fused Lasso Regularization in Time-Lapse MPI Data

The non-negative fused lasso model (2) consists of a convex optimization problem; hence, finding a global minimizer is, in principle, a tractable problem. For small system matrices A – as they appear for example in the 1D MPI setup – we can use generic solvers for example the Chambolle-Pock algorithm [25]. For large system matrices – in particular, for 3D MPI – the generic solvers have a serious bottleneck: they require the evaluation of the proximal mapping of the data term in each iteration. Recall that the proximal mapping of an extended real-valued functional H is defined by

$$\operatorname{prox}_H(v) = \arg\min_u H(u) + \frac{1}{2}\|u - v\|_2^2. \tag{4}$$

In MPI, $H(u) = Au$ for the non-sparse and non-well structured system matrix A. Hence, evaluation of $\operatorname{prox}_A(v)$ for the system matrix A amounts to the time-consuming solution of a non-sparse linear system of dimension NM. To circumvent this bottleneck, we propose a new minimization method: we utilize a specific finite difference discretization of the TV penalty along with a specific use of a generalized forward backward splitting.

A. Near-Isotropic Discretization Adapted to the Acquisition Geometry

While the explicit formulation of the TV penalty is straightforward in 1D as shown in equation (3) it is more involved in higher dimensions. In 2D, the simplest discretization of the TV term consists of finite differences with respect to both coordinate axes, i.e.,

$$\mathrm{TV}_{\mathrm{2D,aniso}}(u) = \sum_{ij} |u_{ij} - u_{i,j+1}| + \sum_{ij} |u_{ij} - u_{i+1,j}|. \tag{5}$$

Unfortunately, this discretization is anisotropic which may lead to undesired block artifacts (geometric staircasing) in the reconstruction [35]. To prevent such effects, we utilize discretizations yielding near-isotropy. The following scheme has been proposed by the authors in the context of Potts priors [21], [36]. We start with a system of finite differences $\mathcal{N} = \{a_1, \dots, a_S\} \in \mathbb{Z}^2 \setminus \{0\}$ and a set of corresponding positive weights $\omega_1, \dots, \omega_S$. Using these systems, we consider the discretization of the TV prior

$$\mathrm{TV}_{\mathrm{2D}}(u) = \sum_{s=1}^{S} \omega_s \|\nabla_{a_s} u\|_1 = \sum_{s=1}^{S} \sum_{ij} \omega_s |u_{ij} - u_{(i,j)+a_s}|, \tag{6}$$

consisting of a weighted sum of oriented finite differences. Note that the simplest case $\mathrm{TV}_{\mathrm{2D,aniso}}$ in (5) corresponds to $a_1 = (1,0)$, $a_2 = (0,1)$ and $\omega_1 = \omega_2 = 1$. A reasonable,

more isotropic, finite difference system is given by

$$\mathcal{N}_{2D} = \{(1,0),(0,1),(1,1),(1,-1),\\ (2,1),(2,-1),(1,2),(1,-2)\}, \tag{7}$$

see [35]. It contains finite differences in axial, diagonal, and "knight-move" directions (referring to the moves of a knight in chess). In [21], the following weights have been derived

$$\omega_s = \begin{cases} \sqrt{5}-2, & \text{for} s = 1,2, \\ \sqrt{5}-\frac{3}{2}\sqrt{2}, & \text{for} s = 3,4, \\ \frac{1}{2}(1+\sqrt{2}-\sqrt{5}), & \text{for} s = 5,\ldots,8. \end{cases} \tag{8}$$

We briefly discuss the gain of this discretization over the anisotropic one (5). First note that a neighborhood system along with the weights gives rise to a norm $\|a\|_{\mathcal{N}}$ given for $a \in \mathbb{R}^2$ by $\|a\|_{\mathcal{N}} = \sum_{s=1}^{S} \omega_s |\langle a, a_s\rangle|$. The above weights are constructed such that $\|a_s\|_{\mathcal{N}}$ coincides with the Euclidean norm $\|a_s\|_2$ for all vectors a_s in the neighborhood system [21]. With these weights, the ratio of the longest and the shortest unit vector is only about 1.03. Thus, this discretization can be considered as almost isotropic. For comparison, the ratio is as high as $\sqrt{2} \approx 1.41$ for the anisotropic discretization.

In 3D, we have to deal with the additional challenge that the sampling rate along the third dimension, Δz, is typically different from that of the other two dimensions, Δx and Δy. Concretely, the acquisition setup of the utilized MPI scanner senses the object in steps of $\Delta x = 2$ mm in x-direction, $\Delta y = 2$ mm in y direction, and $\Delta z = 1$ mm in z-direction. Hence the size of a voxel is $2 \times 2 \times 1$ mm^3. To account for this, we adopt a discretization developed in our work [22] for Potts priors. Here, we briefly recall the approach. As in 2D, we use a discretization of the form

$$\mathrm{TV}_{3D}(u) = \sum_{s=1}^{S} \omega_s \|\nabla_{a_s} u\|_1 = \sum_{s=1}^{S} \sum_{ijk} \omega_s |u_{ijk} - u_{(i,j,k)+a_s}|. \tag{9}$$

A reasonable finite difference system for 3D is given by

$$\mathcal{N}_{3D} = \{(1,0,0),(0,1,0),(0,0,1),\\ (1,1,0),(1,-1,0),(1,0,1),\\ (1,0,-1),(0,1,1),(0,1,-1),\\ (1,1,1),(1,1,-1),(1,-1,-1),(-1,1,-1)\} \tag{10}$$

which corresponds to the 26-connected neighborhood. Let δ be the vector consisting of the three face areas of a voxel, i.e., $\delta = (\Delta y \Delta z, \Delta x \Delta z, \Delta x \Delta y)$. We have proposed to construct the weights ω_i as minimizers of the constrained least squares problem

$$\min_{\omega} \ \|T\omega - q\|_2^2, \quad \text{s.t. } \omega \geq 0. \tag{11}$$

Here, T is the $S \times S$ matrix given by $T_{st} = |\langle a_s, a_t\rangle|$, and $q_s = (\sum_{i=1}^{3} (\delta_i \cdot (a_s)_i)^2)^{1/2}$. The problem (11) can, for example, be solved by using an active set method [37].

As the ℓ_1-penalty does not depend on neighborhood relations we use the standard discretization $\|u\|_1 = \sum_{ij} |u_{ij}|$ for 2D and $\|u\|_1 = \sum_{ijk} |u_{ijk}|$ for 3D. To summarize, we propose to discretize the fused lasso as

$$u^{\#} = \arg\min_{u \geq 0} \ \alpha \sum_{s=1}^{S} \omega_s \|\nabla_{a_s} u\|_1 + \beta \|u\|_1 + \frac{1}{2}\|Au - f\|_2^2, \tag{12}$$

with the neighborhood systems in (7), (10) and the weights in (8), (11), for 2D and 3D, respectively.

We have described the weight design for nonequal voxel side lengths in the 3D setup. Nonequal pixel side lengths may also occur in a 2D setup if the gradients of the selection field are not approximately equal. The proposed weight design can be adapted to 2D by simply solving (11) using the neighborhood system (7), the design matrix $T_{st} = |\langle a_s, a_t\rangle|$, and the length vector $q_s = (\sum_{i=1}^{2} (\delta_i \cdot (a_s)_i)^2)^{1/2}$.

B. Minimization Using Generalized Forward Backward Scheme

Our next goal is to compute the minimizer of the discrete non-negative fused lasso problem (12). To this end, we first rewrite (12) as

$$u^{\#} = \arg\min_{u} \ \sum_{s=1}^{S} \left(\alpha \omega_s \|\nabla_{a_s} u\|_1 + \frac{\beta}{S}\|u\|_1 \right) \\ + \mathcal{I}_+(u) + \frac{1}{2}\|Au - f\|_2^2, \tag{13}$$

where we use the penalty $\mathcal{I}_+(u)$ to incorporate the constraints into the objective function: $\mathcal{I}_+(u)$ is equal to 0 if $u_{ij} \geq 0$ for all i, j, and equal to ∞ otherwise. Note that omitting $\mathcal{I}_+$ is equivalent to dropping the non-negativity assumption. Using the short-hand notation

$$G_s(u) = \alpha \omega_s \|\nabla_{a_s} u\|_1 + \frac{\beta}{S}\|u\|_1 \quad \text{and} \quad F(u) = \frac{1}{2}\|Au - f\|_2^2,$$

our optimization problem (13) has the form

$$\arg\min_{u} \sum_{s=1}^{S} G_s(u) + \mathcal{I}_+(u) + F(u). \tag{14}$$

We now apply the generalized forward backward scheme of Raguet et al. [23] to our splitting (14): concretely, we apply a gradient descent with respect to the data fitting functional F (forward step) and proximal mappings with respect to the directional fused lasso type functionals G_s and the positivity term $\mathcal{I}_+$ (backward steps). Then, the generalized forward backward scheme for the present image formation model (14) reads

$$z_1^{(k+1)} = z_1^{(k)} + \lambda_k \left(\mathrm{prox}_{\frac{\gamma G_1}{r_1}} \left(2u^{(k)} - z_1^{(k)} - \gamma \nabla F(u^{(k)}) \right) - u^{(k)} \right),$$

$$\vdots$$

$$z_S^{(k+1)} = z_S^{(k)} + \lambda_k \left(\mathrm{prox}_{\frac{\gamma G_S}{r_S}} \left(2u^{(k)} - z_S^{(k)} - \gamma \nabla F(u^{(k)}) \right) - u^{(k)} \right),$$

$$z_{S+1}^{(k+1)} = z_{S+1}^{(k)} + \lambda_k \left(\operatorname{prox}_{\frac{\gamma \mathcal{I}_+}{r_{S+1}}} \left(2u^{(k)} - z_{S+1}^{(k)} - \gamma \nabla F(u^{(k)}) \right) - u^{(k)} \right),$$

$$u^{(k+1)} = \sum_{s=1}^{S+1} r_s z_s^{(k+1)}.$$

Here, the positive numbers r_s, $s = 1, \ldots, S+1$, are weights summing up to one, i.e., $\sum_{s=1}^{S+1} r_s = 1$. Raguet et al. [23] have shown that the generalized forward backward scheme converges to a minimizer if $\delta = 1/L$, $\gamma \in (0, 2\delta)$, and $\lambda_k \in (0, \min(\frac{3}{2}, \frac{1}{2} + \delta/\gamma))$ for all $k \in \mathbb{N}$. Here, L is the smallest Lipschitz constant of ∇F. In our case, $L = \|A^*A\|_{\text{op}} = \sqrt{|\rho_{\max}|}$ where $\rho_{\max}$ is the maximum eigenvalue (in absolute value) of $\tilde{A}^T \tilde{A}$. The particular choice of the above weights r_s and the other algorithmic parameters δ, γ, and λ_k are discussed in Section IV-D.

C. Efficient Computation of the Subproblems

As a first step, we have to compute the gradient with respect to the data term F. A straightforward calculation yields

$$\nabla F(u) = A^*(Au - f). \tag{15}$$

Hence, the gradient step has the computational complexity of a matrix vector multiplication; precisely, it is in $\mathcal{O}(NM)$.

Next, we consider the proximal mapping of the non-negativity enforcing functional $\mathcal{I}_+$. We note that the minimization problem is separable with respect to the voxels. Hence, we get the expression

$$\begin{aligned}(\operatorname{prox}_{\gamma \mathcal{I}_+ / r_{S+1}}(u))_{ij} &= \arg\min_{r \in \mathbb{R}} \gamma \frac{\mathcal{I}_+(r)}{r_{S+1}} + \frac{1}{2}\|r - u_{ij}\|_2^2 \\ &= \max(0, u_{ij}). \end{aligned} \tag{16}$$

The computational complexity of this step is $\mathcal{O}(N)$.

It remains to calculate the proximal mappings for the G_s:

$$\begin{aligned} z_s^{\#} &= \operatorname{prox}_{\gamma G_s / r_s}(v) \\ &= \arg\min_u \frac{\gamma \alpha \omega_s}{r_s} \|\nabla_{a_s} u\|_1 + \frac{\gamma \beta}{r_s S} \|u\|_1 + \frac{1}{2}\|u - v\|_2^2. \end{aligned}$$

The crucial observation is that the optimization problem can be decomposed into one-dimensional subproblems with respect to the path defined by the finite difference vector a_s. For instance, for the direction $a_1 = (1, 0)$ we have

$$\begin{aligned}(z_1^{\#})_{:,j} = \arg\min_{u \in \mathbb{R}^m} &\frac{\gamma \alpha \omega_1}{r_1} \|\nabla_{a_1} u\|_1 + \frac{\gamma \beta}{r_1 S} \|u\|_1 \\ &+ \frac{1}{2}\|u - v_{:,j}\|_2^2, \end{aligned} \tag{17}$$

where $v_{:,i} = (v_{1,i}, \ldots, v_{m,i})$. Hence, we have to solve problems of the form

$$\begin{aligned} v^{\#} = \arg\min_{v \in \mathbb{R}^n} &\alpha' \sum_{i=1}^{n-1} |v_{i+1} - v_i| + \beta' \sum_{i=1}^{n} |v_i| \\ &+ \frac{1}{2} \sum_{i=1}^{n} (v_i - f_i')^2. \end{aligned} \tag{18}$$

Algorithm 1 Proposed Algorithm for Edge Preserving Regularization in Time-Lapse MPI

Input: Acquired data $f_{t=l} \in \mathbb{R}^M$ at time frame $l = 1, \ldots, t_{\max}$, model parameters $\alpha \geq 0$ and $\beta \geq 0$

Output: Reconstructed signal/image sequence $U_{t=1,\ldots,t_{\max}}$ where $U_{t=l} \in \mathbb{R}^{n_1}$ (1D), $U_{t=l} \in \mathbb{R}^{n_1 \times n_2}$ (2D), or $U_{t=l} \in \mathbb{R}^{n_1 \times n_2 \times n_3}$ (3D) for $l = 1, \ldots, t_{\max}$

begin
- $U_{t=0} \leftarrow 0$;
- **for** $l = 1, \ldots, t_{\max}$ **do** // loop over time
  - $u \leftarrow U_{t=l-1}$; // warmstarted initialization
  - **repeat** // main loop for frame $t = l$
    - $y \leftarrow \gamma\, A^*(Au - f)$; // scaled gradient $\nabla F(u)$
    - **for** $s = 1, \ldots, S$ **do** // proximal mappings of G_s
      - $y' \leftarrow 2u - z_s - y$;
      - $y' \leftarrow$ Solve univariate TV problems on y' line-wise along direction a_s using the taut string algorithm with parameter $\alpha' = \frac{\gamma \alpha \omega_s}{r_s}$;
      - $y' \leftarrow \operatorname{ST}_{\frac{\gamma \beta}{r_s S}}(y')$; // soft threshold, cf. (19)
      - $z_s \leftarrow z_s + \lambda_k (y' - u)$; // update step
    - **end**
    - $y' \leftarrow \max(2u - z_{S+1} - y, 0)$; // pointwise maximum
    - $z_{S+1} \leftarrow z_{S+1} + \lambda_k (y' - u)$; // update step
    - $u \leftarrow \sum_{s=1}^{S+1} r_s z_s$; // weighted averaging
    - $U_{t=l} \leftarrow u$;
  - **until** *stopping criterion reached*;
- **end**
- **return** $U_{t=1,\ldots,t_{\max}}$

end

To do so, we first consider the special case $\beta' = 0$. Then, (18) can be solved exactly using the taut string algorithm which has linear complexity [38], [39]. We use the fast implementation of L. Condat [27].[1] Remarkably, the case $\beta' > 0$ can be derived easily from a solution for the case $\beta' = 0$: if a solution u^0 for $\beta' = 0$ is known then the solution for $u^{\#}$ for (18) is given by the soft thresholding operation

$$u_i^{\#} = \operatorname{ST}_{\beta'}(u_i) = \operatorname{sign}(u_i^0) \max(|u_i^0| - \beta', 0), \quad i = 1, \ldots, N, \tag{19}$$

see [26, Proposition 1]. As the soft thresholding has linear complexity as well, we get the total complexity $\mathcal{O}(N)$ for the proximal mappings of $G_1, \ldots, G_S$.

To summarize, the complexity of each iteration is governed by the gradient descend step which is $\mathcal{O}(NM)$.

D. Complete Algorithm

The complete procedure described above is outlined in Algorithm 1. Next we discuss the parameter choice, a warmstarting strategy, and the potential for parallelization.

[1] Implementation available at http://www.gipsa-lab.grenoble-inp.fr/laurent.condat/software.html.

TABLE I
REGULARIZATION PARAMETERS AND NRMSE AS WELL AS SSIM OF THE RECONSTRUCTED IMAGES

Phantom		Non-negative fused lasso				Tikhonov		
Fig. 3		α	β	NRMSE	SSIM	ρ	NRMSE	SSIM
(a)	stenosis	0.0017	0.0014	0.034	0.990	0.0037	0.042	0.519
(b)	ellipses	0.0002	0.0016	0.039	0.983	0.0066	0.044	0.561
(c)	coronal tree	10^{-5}	10^{-5}	0.045	0.969	0.0028	0.051	0.571
Fig. 4								
(b)	5% noise	0.0014	0.0014	0.029	0.993	0.012	0.073	0.360
(c)	10% noise	0.0018	0.0013	0.037	0.989	0.027	0.084	0.386
(d)	15% noise	0.0020	0.0015	0.041	0.986	0.037	0.093	0.379

1) Parameter choice: As algorithmic parameters, we utilize $\gamma = \delta$, $\lambda_k = 1$, and the weights $r_1 = \ldots = r_{S+1} = 1/(S+1)$, which guarantee convergence [23]. The model parameters α, β are adjusted empirically. To do so, it is easier to adjust one parameter after the other than both simultaneously. In our experiments, we observed that the α-parameter has a bigger influence on the visual appearance than β. Therefore, we first determined a reasonable value for α, and then adjusted β in a fine-tuning step. The choice of a stopping criterion mainly depends on the desired application. Here, we stop if the relative change between two iterates, $\|u^k - u^{k+1}\|_2/(\|u^k\|_2 + 10^{-3})$, falls below a tolerance, or if a maximum number of iterations is reached.

2) Warmstarting for time-lapse data: Initializing the algorithm with a rather arbitrary guess such as the zero vector may lead to a larger number of iterations. To reduce the number of iterations, we take advantage of the high temporal resolution of MPI. This implies that there is typically only little difference between two consecutive frames which led us to initialize our iterative method with the result of the previous frame.

3) Parallelizability: Algorithm 1 is highly parallelizable. At the level of a single iteration, the part with the highest computational complexity is the gradient step. The involved matrix vector multiplication can be rowwise distributed to multiple processors. We note that, despite its higher complexity, the gradient step (15) needs less time than the evaluation of the proximal mappings (17) for the problem sizes considered in this work. Regarding the proximal mappings, there are two possibilities for parallelization: first, the $S = 13$ iterations of the s-loop in Algorithm 1 as well as the pointwise maximum can be evaluated all in parallel. Second, if more than 14 processors are available (e.g. on the CPU or GPU), we can distribute the univariate fused lasso solvers as well because they consists only of independent rowwise, columnwise and diagonalwise operations.

V. NUMERICAL EXPERIMENTS

We have implemented our algorithm in Matlab. The experiments were conducted on a desktop computer (Intel Xeon E5, 3.5 GHz, 32 GB RAM). In all experiments, A is the system function corresponding to the specific imaging setup (1D, 2D, or 3D). We compare our results with the state-of-the-art method based on the non-negative Tikhonov model, i.e., model (1) with additional non-negativity constraints. As solver we utilize the Kaczmarz method which has been analyzed in the MPI context in [7]. The choice of the regularization parameters will be explained within the paragraph related to specific experiments. Here, we simulated data according to $f = Av + \eta$, where v denotes the ground truth of size $N = 40 \times 40$, $M = 6532$ is the number of measurements, A is a simulated system matrix of dimension $M \times N$, and η is a vector of Gaussian white noise.

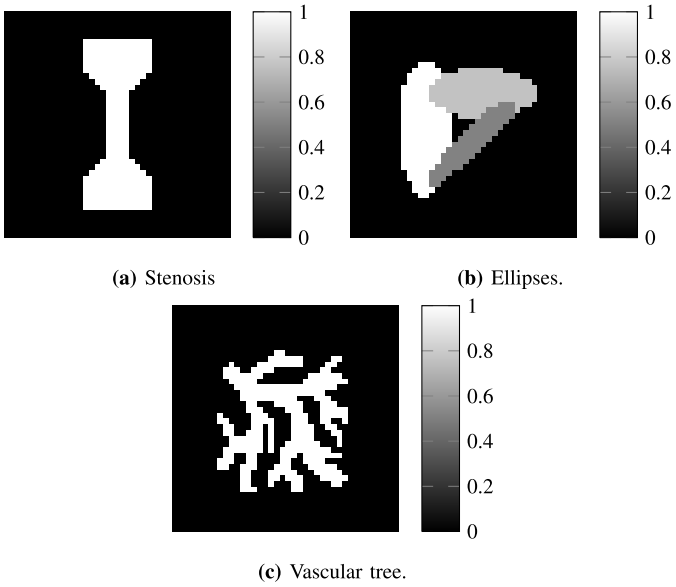

(a) Stenosis **(b)** Ellipses.

(c) Vascular tree.

Fig. 2. Phantoms used for the simulation study.

We first evaluate the reconstruction quality of non-negative fused lasso regularization in comparison to that of non-negative Tikhonov regularization for several different phantoms: a simulated stenosis, overlapping ellipses and a vascular tree, see Fig. 2. The data are corrupted with one percent Gaussian noise. We first determined the optimal model parameters in the sense that best normalized root mean square error (NRMSE) with respect to the ground truth is obtained when iterating until convergence. We note that the model parameters of Tikhonov regularization and fused lasso regularization typically live on different scales. The reconstruction results are shown in Fig. 3, and the corresponding parameters and the errors are given in Table I. For further quantitative comparison, we use the structural similarity index (SSIM) [40]. The SSIM is better suited to perceive visual quality than measures based on the L^2 error as it takes the similarity of local structures into account. The SSIM is bounded from above by 1 and a higher SSIM means a

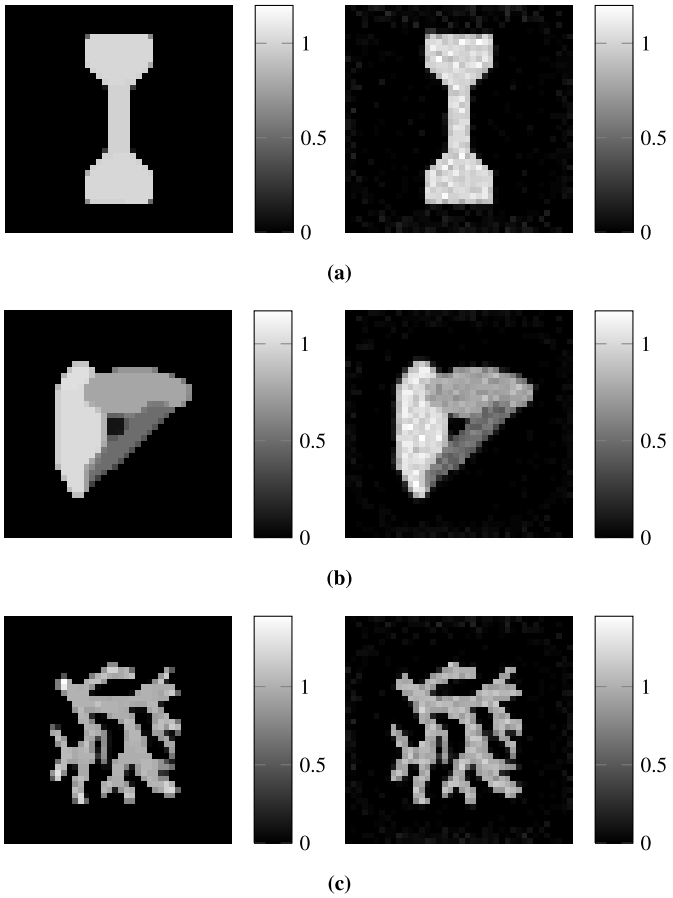

Fig. 3. Comparison between non-negative fused lasso reconstruction (left column, proposed method) and Tikhonov reconstruction with non-negativity constraint (right column) for noisy data corrupted with 1 percent Gaussian noise. (See Table I for the regularization parameters, the normalized root mean square error and structural similarity index.)

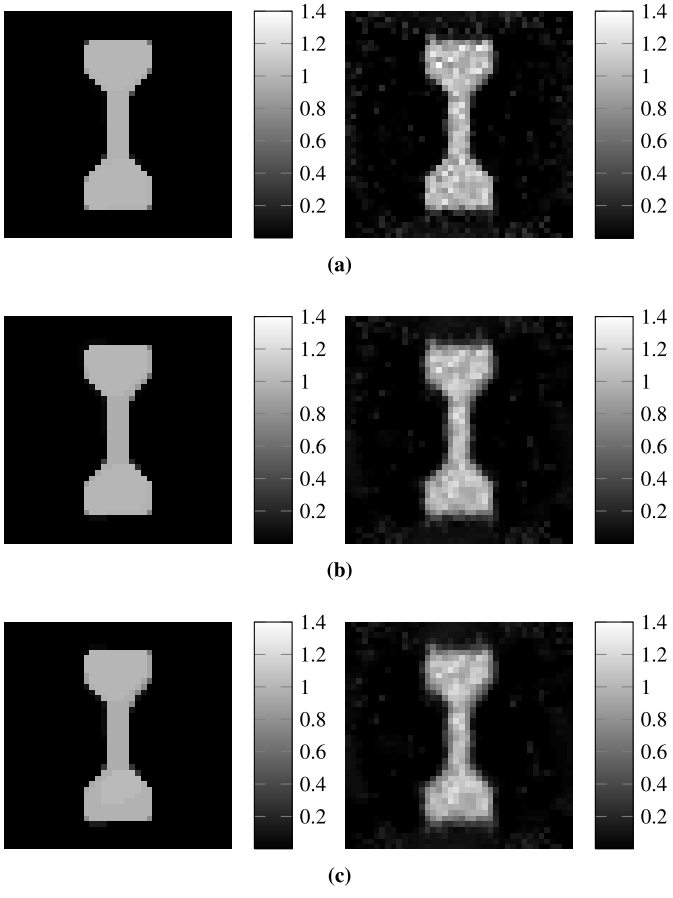

Fig. 4. Non-negative fused lasso reconstruction (left column, proposed method) and non-negative Tikhonov reconstruction (right column) from noisy data corrupted with 5, 10, and 15 percent noise (from top to bottom). We observe that the fused lasso method recovers the sharp boundaries and the spatial homogeneity even for high noise levels. (See Table I for the regularization parameters, the NRMSE and SSIM.)

better reconstruction quality. Here, we use Matlab's function `ssim` with standard parameters for the computation of the SSIM. In all three cases, the non-negative fused lasso solution provides better results than the baseline method, both with respect to visual inspection, to the NRMSE, and to the SSIM.

Next we compare the robustness regarding higher noise levels. To this end, we corrupted the data with 5, 10, and 15 percent Gaussian noise. As before, we determined the optimal parameters with respect to the NRMSE. The reconstruction results are shown in Fig. 4. We observe that even in the case of 15 percent noise, the fused lasso reconstruction retains the homogeneity and the sharp boundaries of the object.

We further compare the sensitivity to the regularization parameters. In Fig. 1, we can qualitatively observe in the onedimensional setup that fused lasso provides satisfactory reconstructions for a broad parameter range of α and β. Next we perform a quantitative comparison in the twodimensional setup. As mentioned earlier, the α-parameter has largest influence on the result; hence we focus on sensitivity for this parameter. In Fig. 5, we plot the NRMSE over the regularization parameters for the fused lasso and the Tikhonov method for two different noise levels. In comparison with the non-negative Tikhonov solution, a wide range of α permits

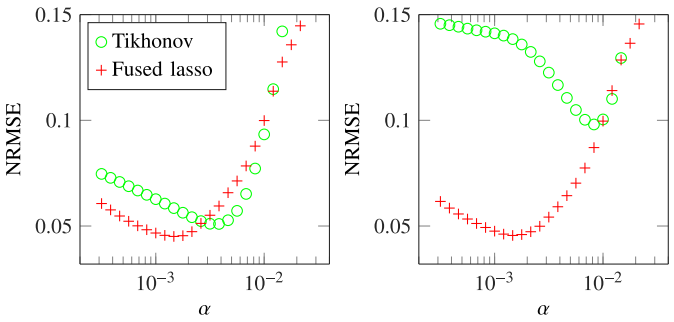

(a) 1 percent noise. **(b)** 5 percent noise.

Fig. 5. Illustration of the optimal NRMSE in dependence of the regularization parameter α in the case of non-negative fused lasso regularization (with $\beta = 0$) and non-negative Tikhonov regularization with non-negativity constraint for the data from Fig. 3 a (left) and Fig. 4 a (right).

to obtain better image quality in the case of low noise. For stronger noise, almost any choice of α would perform better than Tikhonov regularization.

Eventually, we give a more detailed description of the experimental setup of the Fig. 1. A 1D measurement sequence directed in y direction was applied using a drive-field strength

of 14 $\mathrm{mT}\mu_0^{-1}$ and a gradient strength of 0.75 $\mathrm{Tm}^{-1}\mu_0^{-1}$ in y direction. The phantom consists of two homogeneously filled rods of diameter 4 mm and 10 mm length in a 5 mm distance to each other. The excitation with the FFP along a 1D line intersecting the long axis of both rods perpendicularly projects the phantom to two homogeneous spots of diameter 4 mm in a 5 mm distance to each other. One rod was filled with undiluted Resovist, while the other had two-fold dilution. Thus, an ideal reconstruction consists of one plateau of diameter 4 mm, and, in 5 mm distance, another plateau of diameter 4 mm with half of the particle concentration. The system matrix has been measured for a "pixel" resolution of 1 mm, and it has the dimension M = 38 and N = 49. For computation of the fused lasso solution, we have used Algorithm 1 for the one-dimensional case, where in particular $S = 1$ and the only weight $\omega_1 = 1$.

VI. In-Vitro Angioplasty of a Stenosis

It is a promising application of MPI to visualize instruments for cardiovascular intervention [4], [5]. Here, we demonstrate the advantages of our method in an experimental medical setup, the tracking of a balloon catheter during an in-vitro angioplasty. A stenosis is a narrowing of a blood vessel which can lead to stroke or cardiovascular diseases such as angina or myocardial infarction [41]. It can be treated by introducing a balloon catheter into the affected blood vessel and widening the narrowed or obstructed parts. Here, we use our reconstruction method for immediate verification of a successful intervention.

A. Materials and Methods

Experiments are carried out using a preclinical MPI scanner from Philips/Bruker (Ettlingen, Germany). A 3D measurement sequence is used (selection field gradient: 1.5 $\mathrm{Tm}^{-1}\mu^{-1}$ in z direction and 0.75 $\mathrm{Tm}^{-1}\mu^{-1}$ in x and y direction, drive field amplitude 14 $\mathrm{mT}\mu_0^{-1}$ in all three directions) to capture the in-vitro angioplasty. The repetition time of 21.542 ms is determined by the density of the trajectory, which is not adjustable for the scanner used. In total the scanner measured 20000 successive frames without averaging, which amounts to a total measuring time of 7 min and 10 s. For reconstruction a system matrix $A \in \mathbb{R}^{M,N}$ with $M = 13104$ and $N = 25 \times 25 \times 25$ is used. It was measured with a $2 \times 2 \times 1$ mm^3 ferucarbotran (Resovist ®, FUJIFILM RI Pharma Co., Ltd., Japan) filled delta sample averaged over 30 drive field cycles at each position. A vessel phantom was build from a polyvinyl chloride tube with an inner diameter of 4 mm. A partial ligature of the tube using a silk suture material realized the stenosis. During the MPI measurement a balloon catheter (Armada 35, 6/20 mm, Abbott Vascular, Santa Clara, USA) was moved to the position of the stenosis. The balloon was then inflated with ferudextran (MM4, TOPASS GmbH, Berlin, Germany) with an iron concentration of 50 mmol(Fe)/l. Since the physical behavior of Resovist and MM4 is highly similar, it is feasible to use a Resovist system matrix for reconstructing MM4 data. This has the advantage that the SNR within the system matrix is better due to the higher base concentration of Resovist compared to MM4. At first, we inflated with a pressure of 4.5 bar to visualize the shape of the stenosis and then to a pressure of 20 bar to dilate the stenosis, which can be seen in Fig. 6. At the end of the measurement, the catheter is deflated. As before, the baseline method is the Tikhonov/Kaczmarz method with non-negativity constraints where we used the regularization parameter $\rho = 3.14 \cdot 10^8$. For the proposed method, we found empirically that the parameters $\alpha = 0.001$ and $\beta = \alpha/4$ yield a reasonable tradeoff between noise suppression and preservation of relevant structures. We utilize row normalization weights since it improved the image quality and greatly reduced the number of necessary iterations. We have set the stopping tolerance to $5 \cdot 10^{-3}$, and the maximum number of iterations to 50, where typically the first criterion applies.

B. Results

In Fig. 6, we show selected frames of the recorded sequence. More precisely, we show a section of 651 consecutive frames (frames 350– 1000) which contain the relevant phases, i.e. the inflation phase starting around frame 380, and the deflation phase starting around frame 940. The stenosis vanishes near frame 660. The complete sequence is provided in the supplementary material. In the figure, we visually compare the reconstructions obtained by the baseline method and by the proposed method w.r.t. to the maximum intensity projections in z-direction, 3D surface renderings, and the time evolution of the central axial section of the catheter. Quantitatively, we compare the signal-to-noise ratio which is given by the ratio of the mean intensity over a signal region and the standard deviation of the noise, i.e., $\mathrm{SNR} = \mu_{\mathrm{signal}}/\sigma_{\mathrm{noise}}$ where we use decibel as unit. We compute the mean of the signal μ_{signal} as the mean intensity over the catheter, and the standard deviation of the signal-free region. We utilize here frame number 800 where the catheter is fully inflated. The baseline reconstruction gives a signal-to-noise ratio $\mathrm{SNR}_{\mathrm{baseline}} = 14.1\mathrm{dB}$. Using the proposed method, we obtain the significantly higher ratio of $\mathrm{SNR}_{\mathrm{proposed}} = 30.0$ dB. We also observe that the catheter is more homogeneous: the variance on the catheter is 0.007 for the reference reconstruction and only 0.001 for the proposed method. The higher regularity of the proposed reconstruction leads to a smoother 3D rendering than the baseline approach. For the rendering, we use the Matlab function `isosurface`. Seen over time, the proposed method allows for easier identification of the time point when the stenosis is vanishing.

The higher quality comes at the cost of higher computational effort. Our implementation needs in average 5.0 seconds for one frame which is around seven times slower than the state-of-the-art reconstruction (0.7 seconds per frame). We note that the proposed method and the baseline method have been implemented in Matlab without any explicit parallelization. Thus the reconstruction times are directly comparable.

VII. Discussion

The conducted simulation study showed that the proposed method based on the non-negative fused lasso yields significantly higher reconstruction quality for MPI than the currently

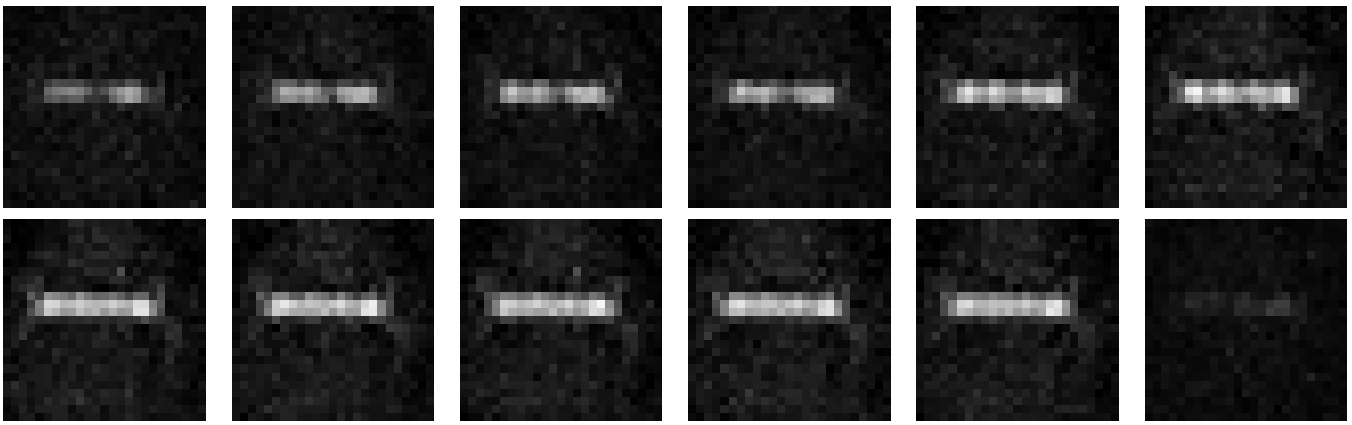

(a) Baseline method (Maximum intensity projection along z-axis, showing frames $400, 450, \ldots, 950$).

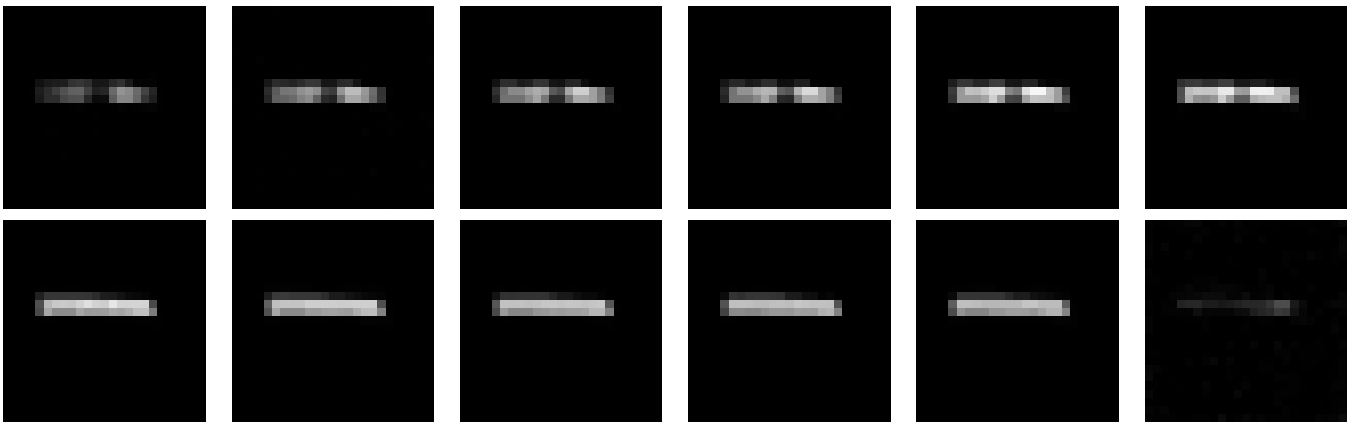

(b) Proposed method (Maximum intensity projection along z-axis, showing frames $400, 450, \ldots, 950$).

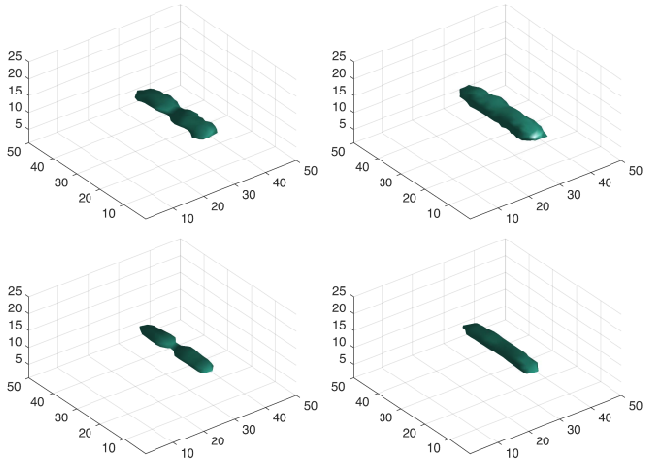

(c) Isosurface rendering of the catheter intensity before (left, frame 500) and after the intervention (right, frame 800). The unit of the coordinate system is millimeter. *Top:* baseline method; *Bottom:* proposed method.

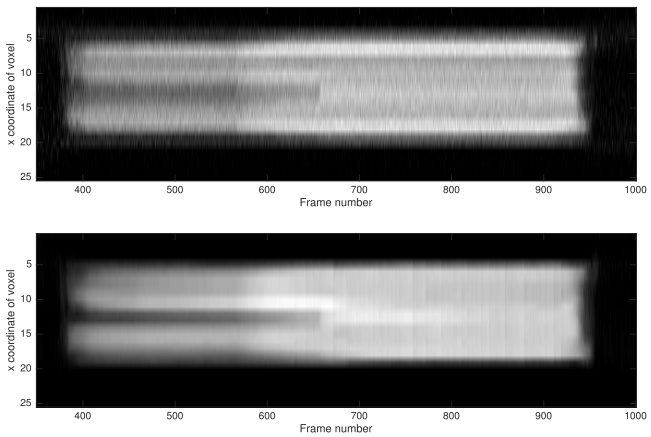

(d) Intensity profile of one-dimensional section at the central axis of the catheter over the time. *Top:* baseline method; *Bottom:* proposed method.

Fig. 6. Tracking of an in-vitro angioplasty using MPI: A balloon catheter is placed within a vessel phantom with a stenosis and dilated using an MPI tracer. The phantom consists of a tube with a narrowing in the center. We observe the disappearance of the narrowing between frame 650 and 700 indicating successful intervention. The 3D images have 25^3 voxels with a size of $2 \times 2 \times 1$ mm each. Compared to the baseline approach, our method has significantly less noise while all relevant structures are preserved. Also, the proposed reconstruction better reflects the homogeneous particle concentration within the balloon. In the new approach edges are displayed sharply (a,b,d). Therefore, the 3D rendering gives a smoother, more realistic shape and captures the real extend of the stenosis (c). As a consequence, when expanding the balloon the narrowing can be seen clearer allowing a more accurate visual estimation of its extend (images 5 to 7 in subfigures a and b).

used reconstruction method based on non-negative Tikhonov regularization. In particular, more noise is suppressed while the relevant structures, in particular the edges, are preserved. The edge preserving aspect could be seen most notably at higher noise levels. Also in the medical application, the angioplasty, our method gives higher reconstruction quality. This has

two important advantages. First, for volume visualization of 3D vessel trees using isosurfaces it is highly important that the background noise is low and that the edges are sharp. Since MPI provides volume data with high temporal resolution this will be an important advantage compared to the currently used digital subtraction angiography (DSA), which only provides projections for navigation. Second, sharp edges are crucial for the quantification of stenosis degree and distance measurements in general. Overall, the higher image quality leads to a higher level of confidence for the clinician for detecting the stenosis, placing the catheter and eventually performing the angioplasty.

Next we discuss current limitations. It is well-known that TV regularization may lead to so called staircasing effects which refers to the phenomenon that linear trends in the underlying image are reconstruced in a blocky fashion; see e.g. [42], [43]. If the underlying signal consists of regions which are of approximately homogeneous density, the negative effects of staircasing are relatively low. If staircasing gets an issue in practice, it can be mildened by using higher order TV-type regularization techniques such as total generalized variation (TGV) [43], [44] or by Mumford-Shah regularization [45]–[47]. Another issue to discuss is the iteration reduction by warmstarting. Here, sudden and large intensity changes in a pixel can cause blurry regions near that pixel. Currently, we have to increase the number of iterations in such a case. However, in the studied target application the intensity changes from frame to frame are moderate so that a moderate number of iterations leads to a satisfactory result. In particular, the result with warmstarting is closer to the minimizer than the result obtained by initialization with zero.

The minimization of the target functional is based on the generalized forward backward scheme of Raguet et al. [23]. However, we use a different splitting approach which – in contrast to [23] – leads to univariate fused lasso problems. We further note that one could employ a Potts prior instead of the TV prior for the target application, as the underlying images are approximately piecewise constant. An advantage of Potts regularization is that it provides directly a segmentation [21]. On the flipside, the Potts model is nonconvex, and it is therefore computationally more demanding.

VIII. Conclusion and Future Research

In this work, we have developed an algorithmic framework for noise reducing and edge preserving reconstruction for magnetic particle imaging. First, we have motivated to use the non-negative fused lasso as prior. Then, we have presented a discretization of the prior adapted to the anisotropic gradient of the MPI selection field. Based on this, we have proposed a specific splitting of the functional which allowed us to invoke a generalized forward backward scheme in a way that no linear systems of equations has to be solved in the iteration. This avoids inner iterations. In particular, the proposed algorithm essentially consists of a single loop where up to 50 iterations have turned out to be sufficient in practice. The essential operations are two matrix-vector multiplications and thirteen univariate pathwise fused lasso solvers which are of linear complexity in the number of voxels. A series of numerical experiments has demonstrated that the non-negative fused lasso suppresses more noise, and, at the same time, better preserves the edges than the currently used reconstruction method based on non-negative Tikhonov regularization. The proposed method also gives higher reconstruction quality for the prototypical medical application of angioplasty at an only moderately higher computational effort.

In a future work, we plan to speed-up our implementation by the following two steps: implementation in C/C++ and parallelization based on OpenMP for multicore CPUs and based on CUDA for the graphics processing unit. Depending on the utilized setup, speedups in the range of 10-100 seem to be feasible which would result in around 2-20 frames per second in the 3D setup.

Acknowledgment

The authors would like to thank L. Condat for making his implementation of the taut string algorithm publicly available.

References

[1] B. Gleich and J. Weizenecker, "Tomographic imaging using the nonlinear response of magnetic particles," *Nature*, vol. 435, no. 7046, pp. 1214–1217, Jun. 2005.
[2] R. M. Ferguson *et al.*, "Magnetic particle imaging with tailored iron oxide nanoparticle tracers," *IEEE Trans. Med. Imag.*, vol. 34, no. 5, pp. 1077–1084, May 2015.
[3] J. Weizenecker, B. Gleich, J. Rahmer, H. Dahnke, and J. Borgert, "Three-dimensional real-time in vivo magnetic particle imaging," *Phys. Med. Biol.*, vol. 54, no. 5, p. L1, 2009.
[4] J. Haegele *et al.*, "Magnetic particle imaging: Visualization of instruments for cardiovascular intervention," *Radiology*, vol. 265, no. 3, pp. 933–938, 2012.
[5] J. Haegele *et al.*, "Magnetic particle imaging (MPI): Visualization and quantification of vascular stenosis phantoms," in *Proc. 4th Int. Workshop Magn. Particle Imag. (IWMPI)*, 2014, pp. 57–58.
[6] T. Knopp, S. Biederer, T. Sattel, and T. M. Buzug, "Singular value analysis for magnetic particle imaging," in *Proc. IEEE Nucl. Sci. Symp. Med. Imag. Conf.*, Oct. 2008, pp. 4525–4529.
[7] T. Knopp *et al.*, "Weighted iterative reconstruction for magnetic particle imaging," *Phys. Med. Biol.*, vol. 55, no. 6, p. 1577, 2010.
[8] L. I. Rudin, S. Osher, and E. Fatemi, "Nonlinear total variation based noise removal algorithms," *Phys. D, Nonlinear Phenomena*, vol. 60, nos. 1–4, pp. 259–268, 1992.
[9] A. Chambolle and P.-L. Lions, "Image recovery via total variation minimization and related problems," *Numer. Math.*, vol. 76, no. 2, pp. 167–188, 1997.
[10] R. Tibshirani, " Regression shrinkage and selection via the lasso," *J. R. Statist. Soc. B (Methodol.)*, vol. 58, no 1, pp. 267–288, 1996.
[11] I. Daubechies, M. Defrise, and C. De Mol, "An iterative thresholding algorithm for linear inverse problems with a sparsity constraint," *Commun. Pure Appl. Math.*, vol. 57, no. 11, pp. 1413–1457, Nov. 2004.
[12] M. Ting, R. Raich, and A. O. Hero, III, "Sparse image reconstruction for molecular imaging," *IEEE Trans. Image Process.*, vol. 18, no. 6, pp. 1215–1227, Jun. 2009.
[13] S. H. Keller, C. Svarer, and M. Sibomana, "Attenuation correction for the HRRT PET-scanner using transmission scatter correction and total variation regularization," *IEEE Trans. Med. Imag.*, vol. 32, no. 9, pp. 1611–1621, Sep. 2013.
[14] Y. Liu *et al.*, "Total variation-stokes strategy for sparse-view X-ray CT image reconstruction," *IEEE Trans. Med. Imag.*, vol. 33, no. 3, pp. 749–763, Mar. 2014.
[15] T. Knopp *et al.*, "2D model-based reconstruction for magnetic particle imaging," *Med. Phys.*, vol. 37, no. 2, pp. 485–491, 2010.
[16] L. R. Croft, P. W. Goodwill, and S. M. Conolly, "Relaxation in X-space magnetic particle imaging," *IEEE Trans. Med. Imag.*, vol. 31, no. 12, pp. 2335–2342, Dec. 2012.
[17] J. J. Konkle *et al.*, "A convex formulation for magnetic particle imaging X-space reconstruction," *PLoS ONE*, vol. 10, no. 10, p. e0140137, 2015.

[18] B. Zheng *et al.*, "Magnetic Particle Imaging tracks the long-term fate of in vivo neural cell implants with high image contrast," *Sci. Rep.*, vol. 5, pp. 14055EP-1–14055EP-9, Sep. 2015.

[19] P. W. Goodwill and S. M. Conolly, "The X-space formulation of the magnetic particle imaging process: 1-D signal, resolution, bandwidth, SNR, SAR, and magnetostimulation," *IEEE Trans. Med. Imag.*, vol. 29, no. 11, pp. 1851–1859, Nov. 2010.

[20] R. Tibshirani, M. Saunders, S. Rosset, J. Zhu, and K. Knight, "Sparsity and smoothness via the fused lasso," *J. R. Statist. Soc. B (Statist. Methodol.)*, vol. 67, no. 1, pp. 91–108, 2005.

[21] M. Storath, A. Weinmann, J. Frikel, and M. Unser, "Joint image reconstruction and segmentation using the Potts model," *Inverse Problems*, vol. 31, no. 2, p. 025003, 2015.

[22] M. Storath, D. Rickert, M. Unser, and A. Weinmann, "Fast segmentation from blurred data in 3D fluorescence microscopy," to be published.

[23] H. Raguet, J. Fadili, and G. Peyré, "A generalized forward-backward splitting," *SIAM J. Imag. Sci.*, vol. 6, no. 3, pp. 1199–1226, 2013.

[24] T. Goldstein and S. Osher, "The split Bregman method for L1-regularized problems," *SIAM J. Imag. Sci.*, vol. 2, no. 2, pp. 323–343, 2009.

[25] A. Chambolle and T. Pock, "A first-order primal-dual algorithm for convex problems with applications to imaging," *J. Math. Imag. Vis.*, vol. 40, no. 1, pp. 120–145, 2011.

[26] J. Friedman, T. Hastie, and H. Höfling, and R. Tibshirani, "Pathwise coordinate optimization," *Ann. Appl. Statist.*, vol. 1, no. 2, pp. 302–332, 2007.

[27] L. Condat, "A direct algorithm for 1-D total variation denoising," *IEEE Signal Process. Lett.*, vol. 20, no. 11, pp. 1054–1057, Nov. 2013.

[28] T. Knopp and T. Buzug, *Magnetic Particle Imaging: An Introduction to Imaging Principles and Scanner Instrumentation*. New York: Springer, 2012.

[29] J. Rahmer, J. Weizenecker, B. Gleich, and J. Borgert, "Analysis of a 3-D system function measured for magnetic particle imaging," *IEEE Trans. Med. Imag.*, vol. 31, no. 6, pp. 1289–1299, Jun. 2012.

[30] T. Knopp and A. Weber, "Sparse reconstruction of the magnetic particle imaging system matrix," *IEEE Trans. Med. Imag.*, vol. 32, no. 8, pp. 1473–1480, Aug. 2013.

[31] T. Knopp *et al.*, "Model-based reconstruction for magnetic particle imaging," *IEEE Trans. Med. Imag.*, vol. 29, no. 1, pp. 12–18, Jan. 2010.

[32] M. Kaul *et al.*, "Combined preclinical magnetic particle imaging and magnetic resonance imaging: Initial results in mice," *RoFo, Fortschritte Gebiete Röntgenstrahlen Nuklearmedizin*, vol. 187, no. 5, pp. 347–352, 2015.

[33] J. Rahmer, A. Halkola, B. Gleich, I. Schmale, and J. Borgert, "First experimental evidence of the feasibility of multi-color magnetic particle imaging," *Phys. Med. Biol.*, vol. 60, no. 5, pp. 1775–1791, 2015.

[34] A. Weber, F. Werner, J. Weizenecker, T. M. Buzug, and T. Knopp, "Artifact free reconstruction with the system matrix approach by oversampling the field-free-point trajectory in magnetic particle imaging," *Phys. Med. Biol.*, vol. 61, no. 2, p. 475, 2015.

[35] A. Chambolle, "Finite-differences discretizations of the Mumford–Shah functional," *ESAIM, Math. Model. Numer. Anal.*, vol. 33, no. 2, pp. 261–288, Apr. 1999.

[36] M. Storath and A. Weinmann, "Fast partitioning of vector-valued images," *SIAM J. Imag. Sci.*, vol. 7, no. 3, pp. 1826–1852, 2014.

[37] C. L. Lawson and R. J. Hanson, *Solving Least Squares Problems*, vol. 161. Philadelphia, PA, USA: SIAM, 1974.

[38] E. Mammen and S. van de Geer, "Locally adaptive regression splines," *Ann. Statist.*, vol. 25, no. 1, pp. 387–413, Feb. 1997.

[39] P. Davies and A. Kovac, "Local extremes, runs, strings and multiresolution," *Ann. Statist.*, pp. 1–48, 2001.

[40] Z. Wang, A. C. Bovik, H. R. Sheikh, and E. P. Simoncelli, "Image quality assessment: From error visibility to structural similarity," *IEEE Trans. Image Process.*, vol. 13, no. 4, pp. 600–612, Apr. 2004.

[41] S. Mendis, P. Puska, and B. Norrving, "Global atlas on cardiovascular disease prevention and control," in *World Health Organization in collaboration With the World Heart Federation and the World Stroke Organization*. 2011, pp. 3–18.

[42] T. Chan, S. Esedoglu, F. Park, and A. Yip, "Recent developments in total variation image restoration," *Math. Models Comput. Vis.*, vol. 17, no. 2, p. 2, 2005.

[43] F. Knoll, K. Bredies, T. Pock, and R. Stollberger, "Second order total generalized variation (TGV) for MRI," *Magn. Reson. Med.*, vol. 65, no. 2, pp. 480–491, Feb. 2011.

[44] K. Bredies, K. Kunisch, and T. Pock, "Total generalized variation," *SIAM J. Imag. Sci.*, vol. 3, no. 3, pp. 492–526, 2010.

[45] D. Mumford and J. Shah, "Optimal approximations by piecewise smooth functions and associated variational problems," *Commun. Pure Appl. Math.*, vol. 42, no. 5, pp. 577–685, 1989.

[46] L. Rondi and F. Santosa, "Enhanced electrical impedance tomography via the Mumford–Shah functional," *ESAIM, Control, Optim. Calculus Variat.*, vol. 6, pp. 517–538, Apr. 2001.

[47] K. Hohm, M. Storath, and A. Weinmann, "An algorithmic framework for Mumford–Shah regularization of inverse problems in imaging," *Inverse Problems*, vol. 31, no. 11, p. 115011, 2015.